Tailorable metal-organic framework based thin film nanocomposite membrane for lithium recovery from wasted batteries

Bo Han [1*], Sarah M. Chevrier [1,2], Qingyu Yan[1,3], Jean-Christophe P. Gabriel [1,2,*]

[1] SCARCE Laboratory, Energy Research Institute @ NTU (ERI@N),

Nanyang Technological University, Singapore 637459, Singapore

[2] LICSEN, NIMBE, CNRS, CEA, Université Paris-Saclay, 91191 Gif-sur-Yvette, France

[3]School of Materials Science and Engineering,

Nanyang Technological University, 639798, Singapore

* Correspondence: han.bo@ntu.edu.sg, jean-christophe.gabriel@cea.fr

S1. Materials, chemicals and apparatus

Figure S1 shows the molecular structure of the ionic liquid used in this work. The full terminology and the abbreviation of each ionic liquid are listed below:

1-Ethyl-3-methylimidazolium chloride ($[EMIM]^+[Cl]^-$)

1-Ethyl-3-methylimidazolium bromide ($[EMIM]^+[Br]^-$)

1-Butyl-3-methylimidazolium chloride ($[BMIM]^+[Cl]^-$)

1-Butyl-3-methylimidazolium bromide ($[BMIM]^+[Br]^-$)

1-Butyl-3-methylimidazolium tetrachloroaluminate ($[BMIM]^+[AlCl_4]^-$)

1-Butyl-3-methylimidazolium methanesulfonate ($[BMIM]^+[MeSO_3]^-$)

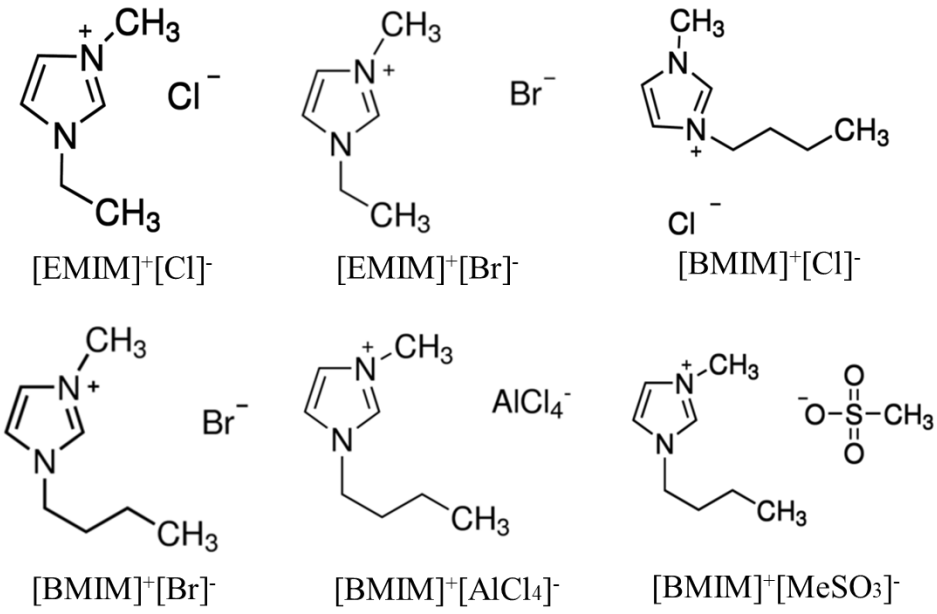

Figure S1: Ionic liquid molecular structures.

Table S1 shows the component analysis of LIBs leaching solution used in this work.

Table S1. Component analysis of the practical LIBs leaching solution.

Solution	Concentration (mg/100 ml)	Ratio (with respect to Li)
Li^{+}	82.92	1
Mn^{2+}	126.78	1.53
Co^{2+}	104.94	1.27
Ni^{2+}	341.74	4.12
Cu^{2+}	3.61	0.04
Fe^{3+}	4.33	0.05
Al^{3+}	5.08	0.05

High pressure stirred cell apparatus

Specially, the commercially available commercially available high-pressure (HP4750) stirred cell provided by STERLITECH is made of 11 main components (as shown in Figure S2(a)) : (1) stainless steel cell body, (2) cell top, (3) cell bottom, (4) cell top coupling, (5) cell bottom coupling, (6) porous stainless stell membrane support disk, (7) 2 O-rings, (8) top Gasket, (9) permeate tube, (10) stir bar assembly, and (11) stir bar. In addition, Figure S2(b) illustrates the typical configuration of a standard stirred cell System. The drawing shows the three major components of the system: the Cell Body with removable top and bottom, Stir Bar Assembly, and Standard Coupling. It is noted that such apparatus has been widely used in membrane-based separation research [1, 2].

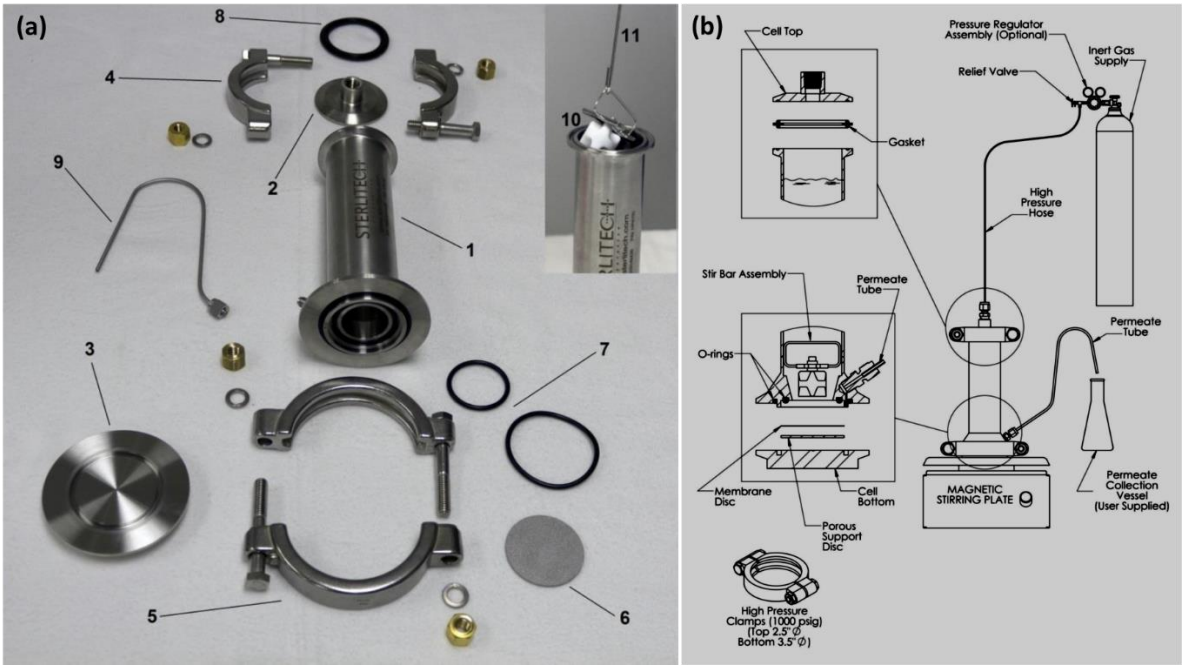

Figure S2: (a) the stirred cell components; (b) schematic system of the stirred cell.

The high pressure stirred cell apparatus for metal ion separation is shown in Figure S2(c). Here, inert gas supply (No.1), pressure regulator (No.2), high pressure hose (No.3), stirred cell (No.4), magnetic stirring plate (No.5), balance (No.6), permeate tube (No.7), permeate collection beaker (No.8) and permeate weight detection (vs time) software (No.9) are labeled for comprehensive understanding.

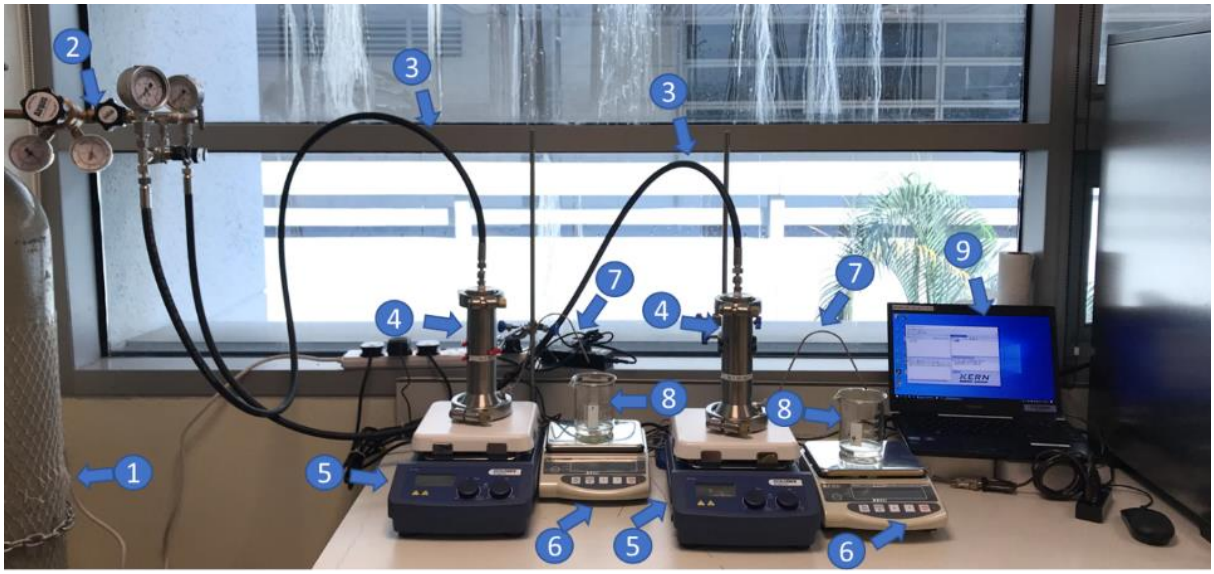

Figure S2(c): Lithium recovery experiment apparatus.

S2. MOF and TFN membrane characterization

S2.1. MOF characterization

Figure S3 shows the Powder X-ray diffraction (PXRD) trends of all the pristine and ionic liquid encapsulated MIL-101 (Cr) MOFs. Similar XRD profiles are found between original and modified MOFs, which synchronize with the standard XRD curve as explained in the main manuscript. Therefore, the structure integrity of the MIL-101 (Cr) nanoparticle is not distorted by the ionic liquid encapsulation work.

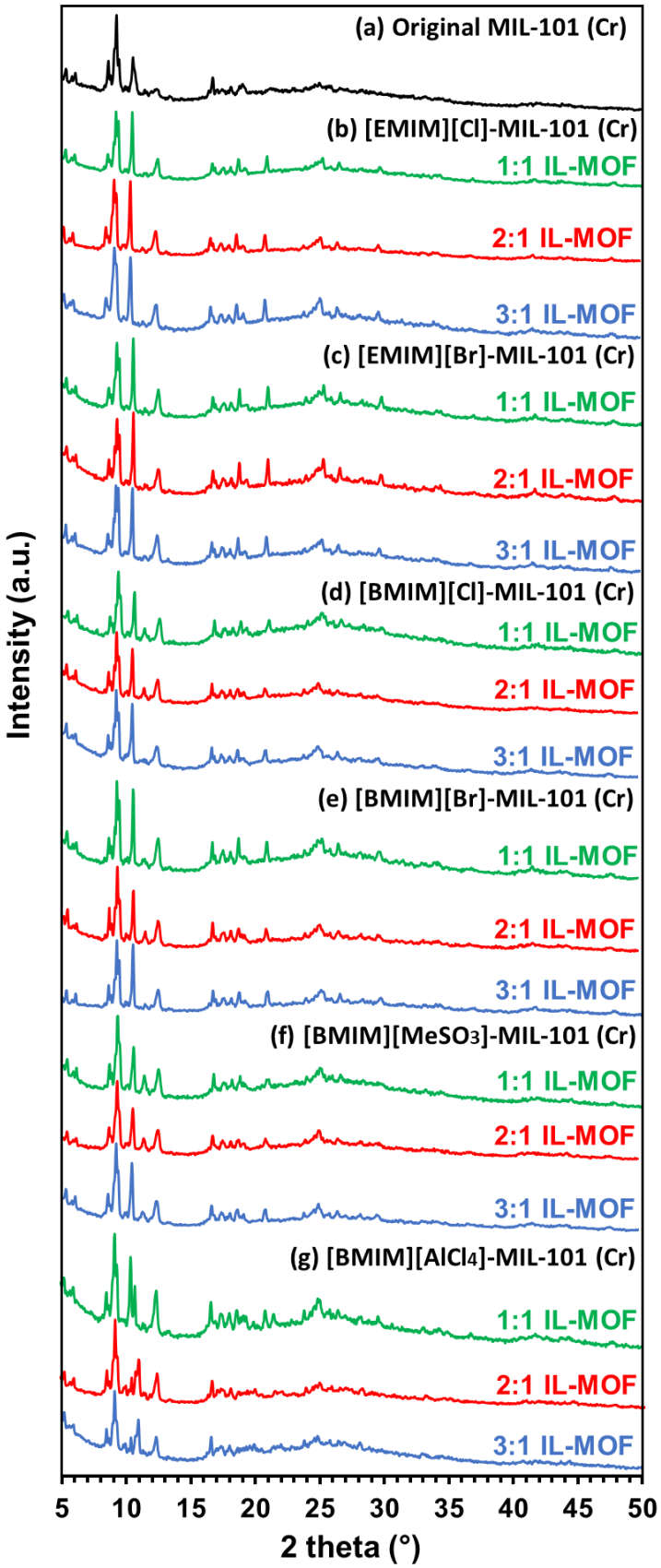

Figure S3: XRD profiles for the original and ionic liquid encapsulated MIL-101 (Cr) MOFs.

The FTIR profiles of all the MIL-101 (Cr) based nanoparticles are displayed in Figure S4. It is observed that besides the original distinct peaks, few extra peaks at certain wavenumber are detected for the modified MIL-101 (Cr). This is mainly because of the new generated chemical bonding from the ionic liquid additives and MOF framework.

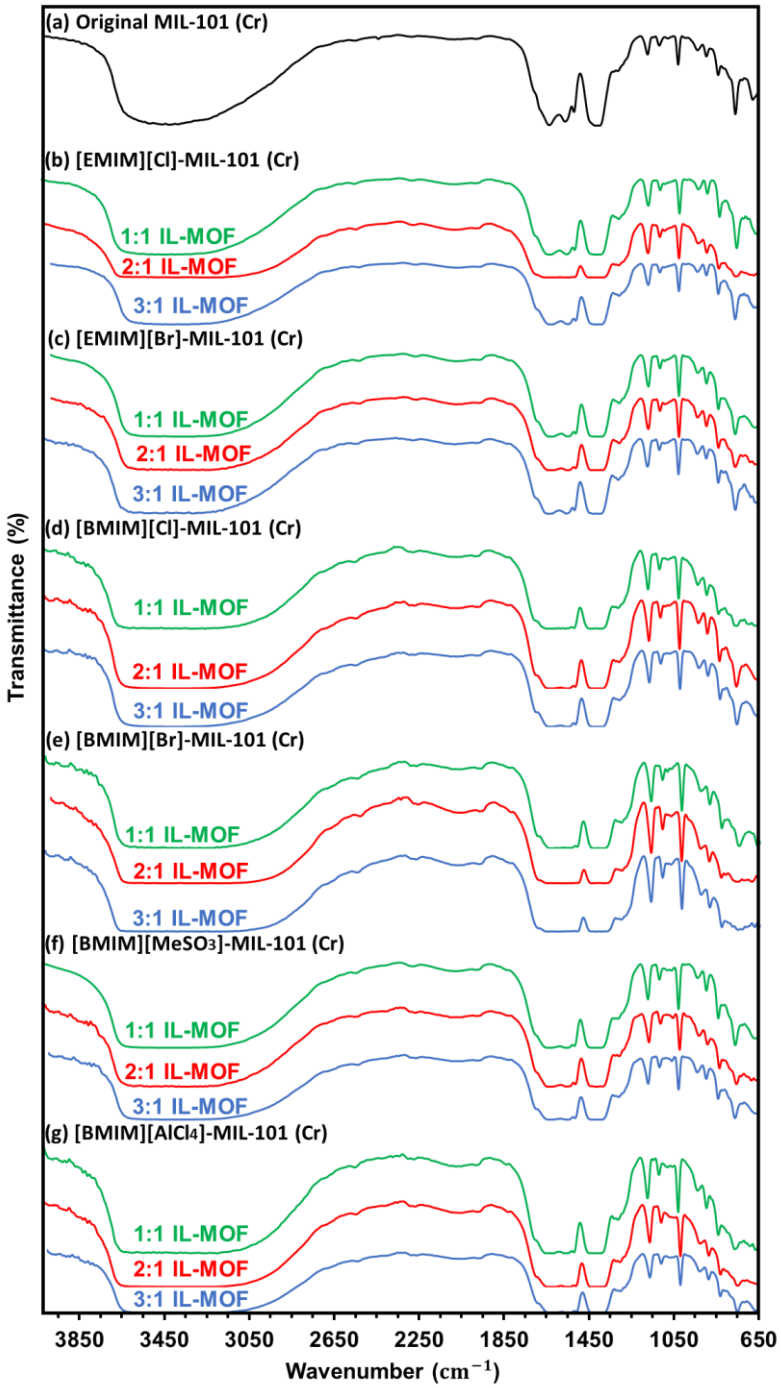

Figure S4: FTIR profiles for original and modified MOFs.

The SEM images of all the ionic liquid encapsulated MIL-101 (Cr) nanoparticles are shown in Figure S5. It is found that the as compared with the parent MOF (as shown in the main manuscript), all the modified MIL-101 (Cr) exhibit similar octahedral shape with comparable size. The SEM images prove that the morphologies of the ionic liquid encapsulated MOF are maintained and the micro-structure of the original MIL-101 (Cr) is not destroyed by ionic liquid encapsulation.

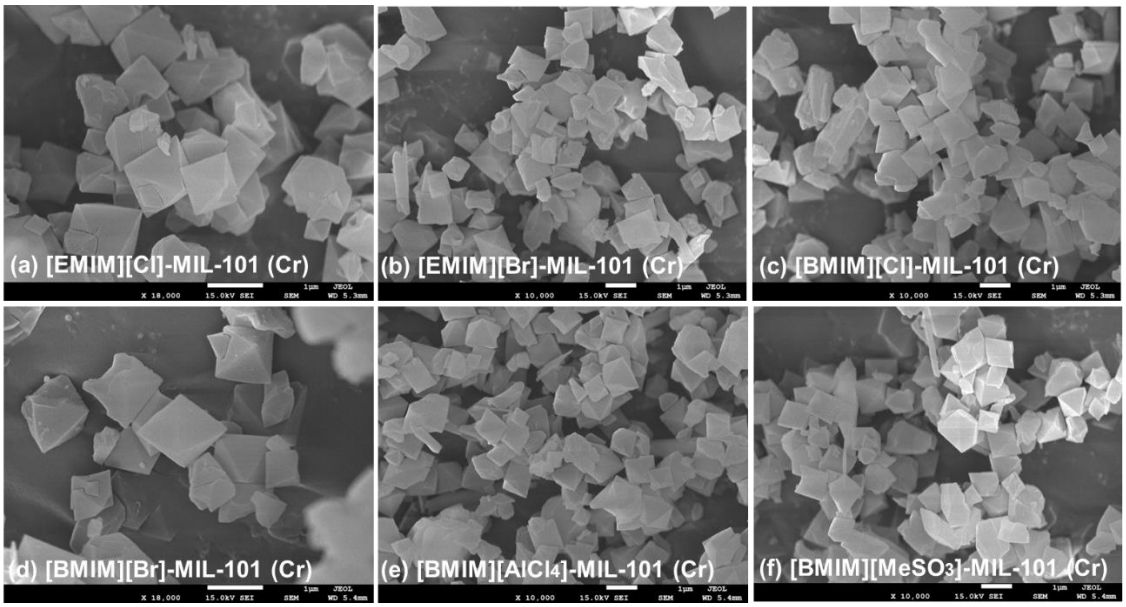

Figure S5: SEM pictures of ionic liquid modified MIL-101 (Cr) MOFs.

Figure S6 show the overall TGA plots of the pristine and modified MIL-101 (Cr) powder. Main findings are summarized as: (i) as the temperature increases, a typical three-step weight loss curve is found for all the MOFs; (ii) the decomposition temperature for all the ionic liquid encapsulated MOF ranges from 330 °C to 370 °C, which indicates that modified MIL-101 (Cr) is thermal stable for meal ion separation applications.

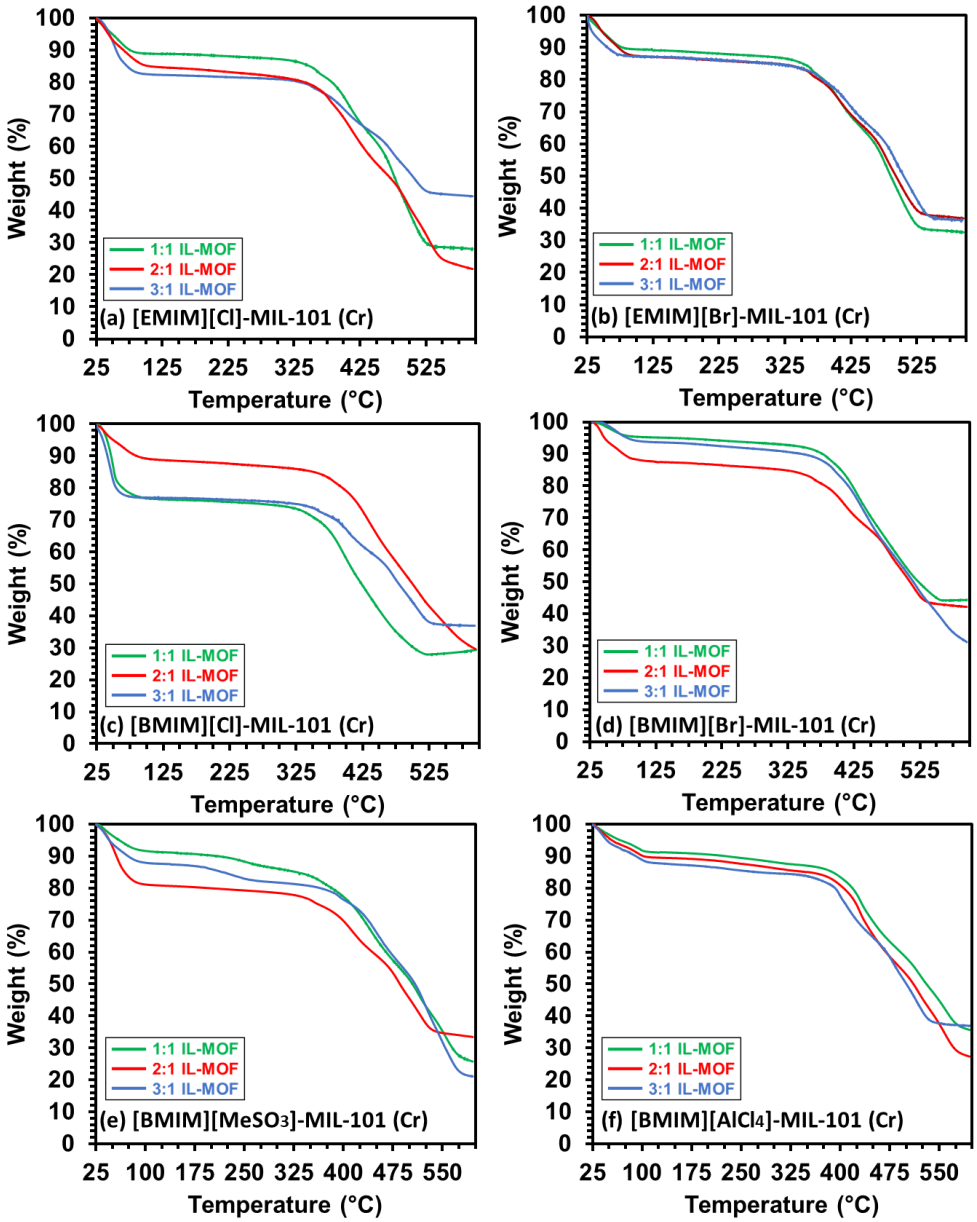

Figure S6: TGA profiles of MIL-101 (Cr) based MOFs.

The porosity information of all the MIL-101 (Cr) based MOFs are furnished in Table S2. As ionic liquid additives are encapsulated into MOF framework, major findings are summarized as: (i) the average pore width of all the MIL-101 (Cr) nanoparticles ranges from 20.17 Å to 21.09 Å; (ii) BET surface area decreases from 2373.3 m^2/g down to 1875.6 m^2/g; (iii) the total pore volume decreases from 1.197 cm^3/g down to 1.042 cm^3/g while the micropore volume increases evidently from 0.14 cm^3/g up to 0.317 cm^3/g. Hence, the micro-porosity is enhanced for modified MIL-101 (Cr).

Table S2. Porosity (BET surface area, pore volume and pore size) of the MIL-101 (Cr) based MOFs.

Samples	Average pore width (Å)	BET surface area (m^2/g)	Micropore volume (V_m, cm^3/g)	Total pore volume (V_t, cm^3/g)	V_m/V_t
MIL-101	20.17	2373.3	0.140	1.197	0.117
1:1 [EMIM][Cl]-MIL-101	20.81	1876.2	0.309	1.068	0.289
2:1 [EMIM][Cl]-MIL-101	20.81	1915.8	0.311	1.093	0.284
3:1 [EMIM][Cl]-MIL-101	20.76	1875.6	0.318	1.064	0.298
1:1 [EMIM][Br]-MIL-101	20.87	1905.5	0.310	1.091	0.284
2:1 [EMIM][Br]-MIL-101	20.82	1942.0	0.315	1.110	0.283
3:1 [EMIM][Br]-MIL-101	20.78	1876.2	0.308	1.070	0.287
1:1 [BMIM][Cl]-MIL-101	20.75	2113.5	0.313	1.096	0.286
2:1 [BMIM][Cl]-MIL-101	20.79	1875.4	0.299	1.071	0.279
3:1 [BMIM][Cl]-MIL-101	20.78	1886.3	0.295	1.081	0.273
1:1 [BMIM][Br]-MIL-101	21.00	1986.8	0.314	1.149	0.274
2:1 [BMIM][Br]-MIL-101	20.91	1963.6	0.307	1.132	0.271
3:1 [BMIM][Br]-MIL-101	20.92	1985.9	0.307	1.145	0.268
1:1 [BMIM][$AlCl_4$]-MIL-101	20.63	2054.5	0.319	1.060	0.301
2:1 [BMIM][$AlCl_4$]-MIL-101	20.64	2067.3	0.310	1.066	0.290
3:1 [BMIM][$AlCl_4$]-MIL-101	20.69	2048.2	0.317	1.060	0.299
1:1 [BMIM][$MeSO_3$]-MIL-101	21.03	2042.4	0.288	1.074	0.268
2:1 [BMIM][$MeSO_3$]-MIL-101	21.09	1975.9	0.287	1.042	0.276
3:1 [BMIM][$MeSO_3$]-MIL-101	21.01	2024.0	0.293	1.063	0.275

S2.2.TFN membrane characterization

Figure S7(a) shows the ATR-FTIR profile of pure PVDF membrane. A large band centred at 3389 cm^{-1} is ascribed to the O-H stretching, also covering the CH2 antisymmetric and symmetric stretching peaks of pure PVDF near 3025 and 2983 cm^{-1} respectively. ATR-FTIR plot of MIL-101 (Cr) based TFN membrane is shown in Figure S7(b)**Erreur ! Source du renvoi introuvable.**. C=O groups vibration (in MIL-101 and in the polyamide layer) are responsible for the band near 1617 cm^{-1}. Peaks in the range of 1400-1600 cm^{-1} correspond to the aromatic ring stretching and can include C-N band of the IP layer. The band at 1392 cm^{-1} is due to the symmetric (O-C-O) vibration caused by the dicarboxylate linker inside the MOF. The bands appearing at 1286 and 1255 cm^{-1} can represent N−H deformation vibration of amide bond formation and C-O elongation of the MOF, respectively. The peak at 1161 cm^{-1} includes the CF2 stretching of PVDF as well as the C-H bending of the MOF aromatic rings, also responsible for the band at 1018 cm^{-1}. The band at 828 cm^{-1} corresponds to the C-H deformation of the MOF's aromatic rings and the one at 747 cm^{-1} is related to the γ(C-H) vibrations of aromatic rings of MIL-101. The characteristic FTIR bands of pure PVDF are not much visible as compared to its profile in Figure S7(a), which can be explained by the penetration depth of the ATR-FTIR, of several microns. In addition, the FTIR profile of the modified MOF (2:1 [BMIM][$AlCl_4$]-MOF) based TFN membrane with the highest lithium selectivity is given in **Erreur ! Source du renvoi introuvable.** S7(c). The same bands as for the FTIR profile of the original MOF are found. The peak at 1617 cm^{-1} is more intense because of C=C and N=C=N stretching of the imidazolium cation ring of the IL. C=C and C=N stretching of the imidazolium ring are also responsible of the bands at 1545 and 1509 cm^{-1}. Symmetric and asymmetric stretching of CH_2 and CH_3 in the IL cause the intensification of the bands at 1470 cm^{-1} and 1440 cm^{-1}. The peak at 1166 cm^{-1} also covers the CH_3-N stretching of $[BMIM]^+$ in addition to the CF2 stretching of PVDF. C-N stretching vibration is present in the band at 829 cm^{-1}. The

peaks at 747 cm^{-1} and the one appearing at 659 cm^{-1} are related to plane and out-of-plane imidazolium bending, respectively.

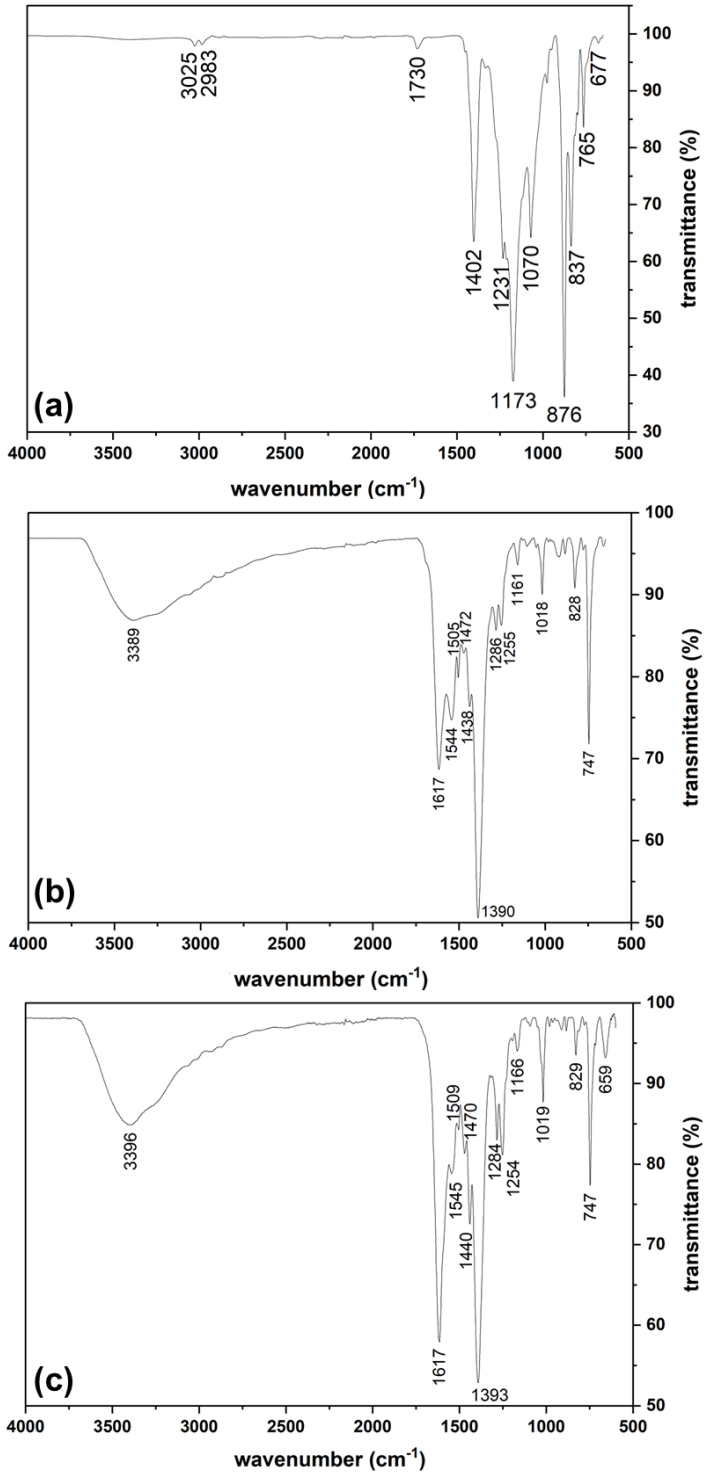

Figure S7: ATR-FTIR profile of (a) pure PVDF membrane; (b) MIL-101 (Cr) based TFN membrane; and (c) 2:1 [BMIM][$AlCl_4$]-MIL-101 based TFN membrane.

The ATR-FTIR profiles for the pure PVDF substrate, original MOF based TFN membrane and all the ionic liquid encapsulated MOF based TFN membranes are shown in Figure S8. The detailed analysis for each distinct peak is presented in the main manuscript and the peak differences between the three types of membranes suggest the successful loading of MOF based nanoparticles on the PVDF surface. The performance change of the TFN membrane could be attributed to many reasons, from the structural change of the nanoparticles to the membrane fabrication methods (such as surface deposition or coating and interfacial polymerization (IP)). In this work, all the membranes are prepared by the IP method using the standard fabrication procedure. The PXRD and FTIR profiles prove the preserved structural integrity of the modified MOFs. All these factors indicate that the improved membrane performance can only be attributed to the ILs guests (tailored pore opening and charge property).

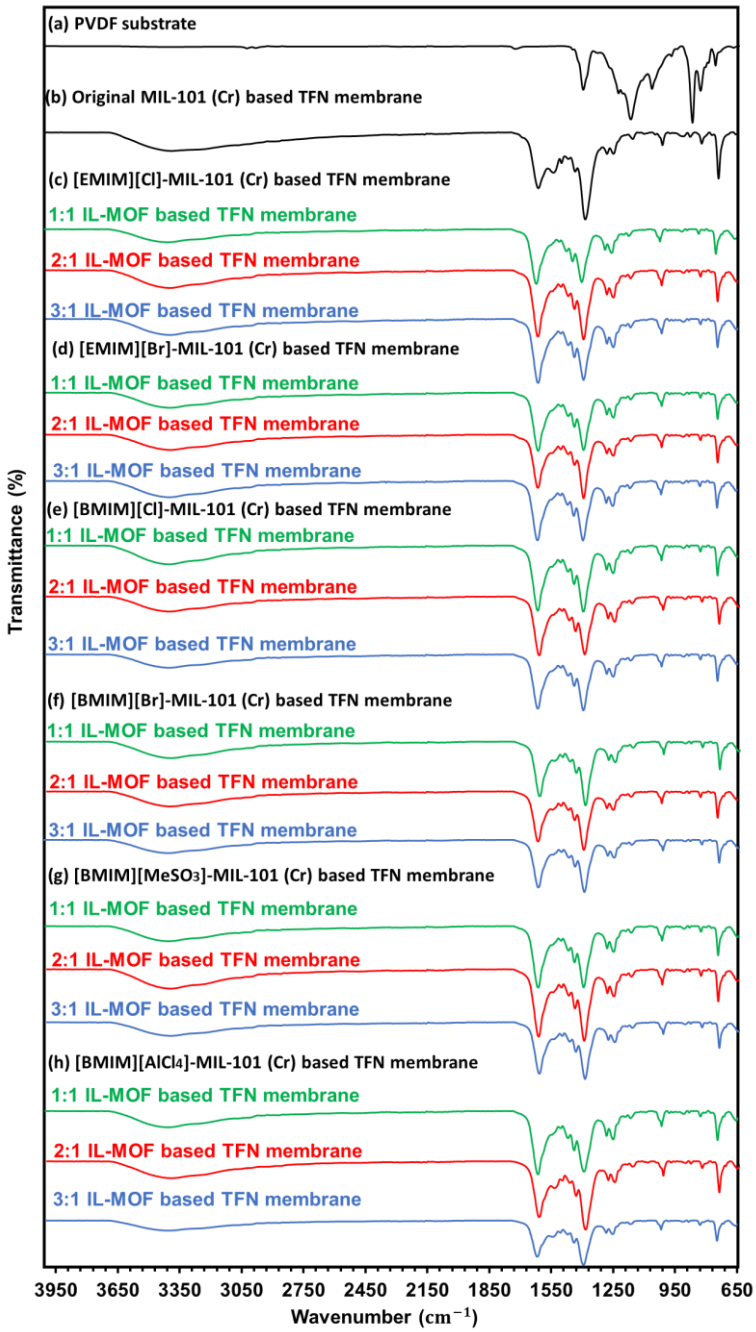

Figure S8: ATR-FTIR profiles of various IL-MOF based TFN membranes.

Figure S9 shows the TGA curves for membranes, from where one can characterize the thermal stability of the pure PVDF substrate, MOF loaded PVDF membrane (without IP reaction) and MOF based TFN membrane (with IP reaction).

The main purpose of showing the TGA profiles of the as-prepared membranes is to prove their promising thermal stability (up to 300 °C), which is quite qualified for metal ion separation process over a wide temperature range.

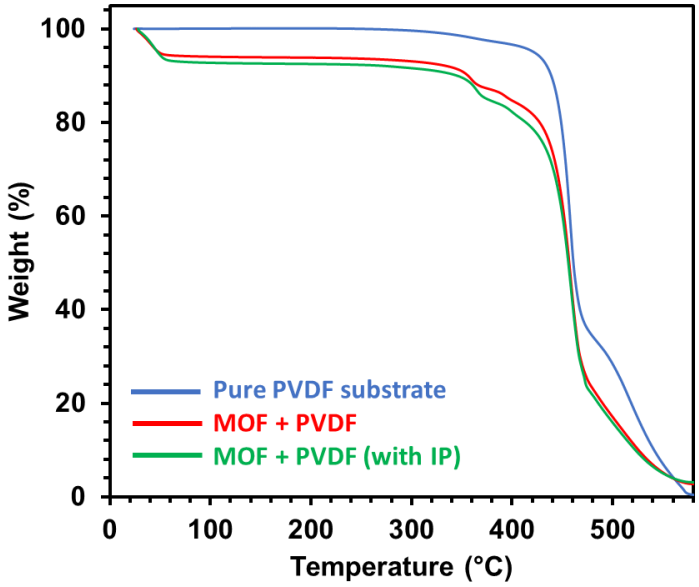

Figure S9: TGA curves for pure PVDF substrate, MOF encapsulated PVDF membrane and MIL-101 (Cr) encapsulated PVDF based TFN membrane (via IP reaction).

Figure S10 shows the surface roughness images for all the original and modified MOF based TFN membranes. The detailed surface roughness parameters are furnished in Table S3 for comprehensive understanding.

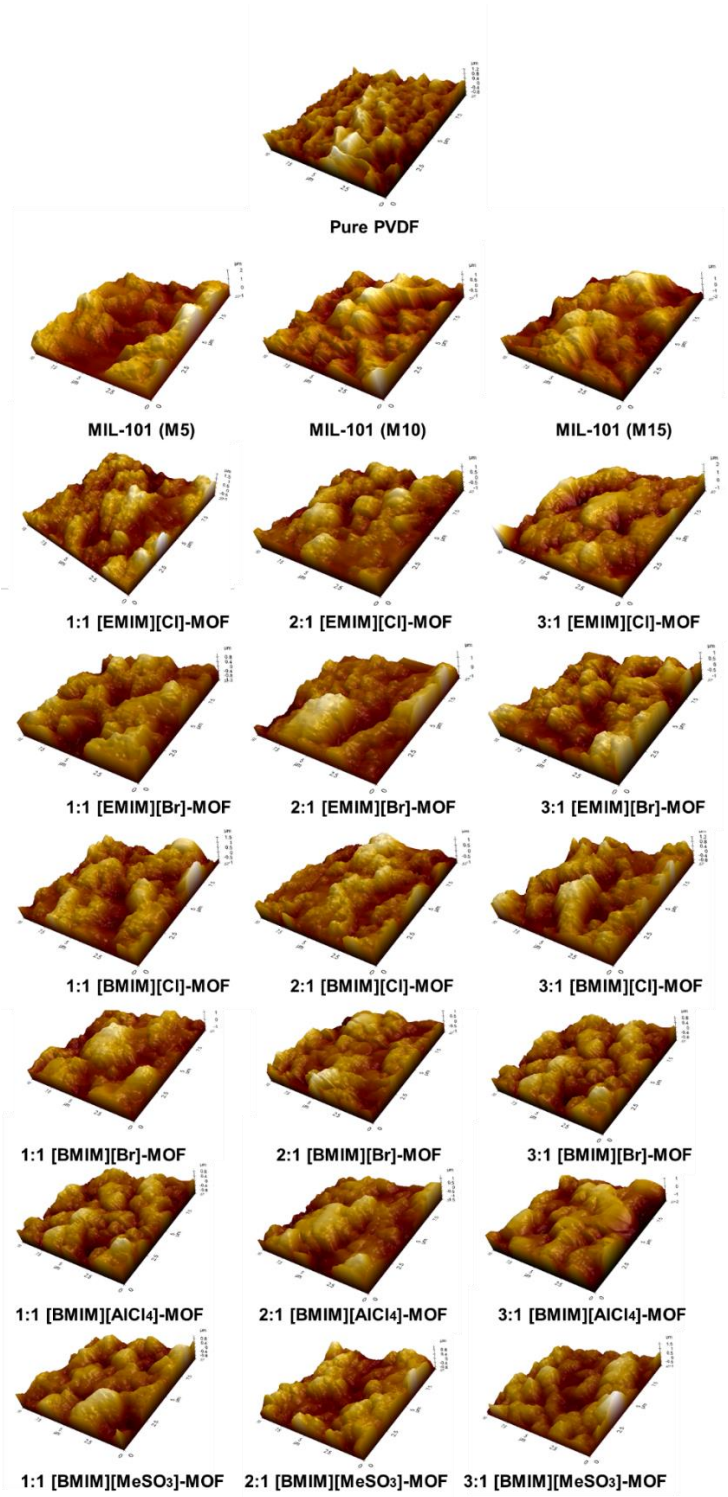

Figure S10: AFM image of all the membranes used in this work.

Table S3: Surface roughness parameters for all the MIL-101 (Cr) based TFN membranes.

MOF type/amount	Rms (µm)	Ra (µm)	Rz (µm)
Pure PVDF membrane	0.313	0.240	2.332
MIL-101 (Cr) (M5)	0.434	0.345	2.524
MIL-101 (Cr) (M10)	0.622	0.519	3.136
MIL-101 (Cr) (M15)	0.705	0.572	4.410
1:1 [EMIM][Cl]-MIL-101	0.362	0.293	2.518
2:1 [EMIM][Cl]-MIL-101	0.443	0.349	2.653
3:1 [EMIM][Cl]-MIL-101	0.502	0.401	3.599
1:1 [EMIM][Br]-MIL-101	0.464	0.375	2.339
2:1 [EMIM][Br]-MIL-101	0.570	0.432	3.024
3:1 [EMIM][Br]-MIL-101	0.401	0.323	2.394
1:1 [BMIM][Cl]-MIL-101	0.436	0.357	2.683
2:1 [BMIM][Cl]-MIL-101	0.360	0.283	2.350
3:1 [BMIM][Cl]-MIL-101	0.431	0.354	2.321
1:1 [BMIM][Br]-MIL-101	0.589	0.479	3.339
2:1 [BMIM][Br]-MIL-101	0.373	0.296	2.358
3:1 [BMIM][Br]-MIL-101	0.321	0.254	2.029
1:1 [BMIM][$AlCl_4$]-MIL-101	0.494	0.397	2.830
2:1 [BMIM][$AlCl_4$]-MIL-101	0.479	0.385	3.049
3:1 [BMIM][$AlCl_4$]-MIL-101	0.412	0.327	2.625
1:1 [BMIM][$MeSO_3$]-MIL-101	0.438	0.356	2.707
2:1 [BMIM][$MeSO_3$]-MIL-101	0.393	0.334	2.114
3:1 [BMIM][$MeSO_3$]-MIL-101	0.404	0.325	2.244

The water contact angle snapshots of all the membranes investigated in this work are summarized in Figure S11. In addition, the contact angles are furnished in Table S4 for comparison purpose. Overall, the wettability of all the membranes used in this work could be ranked as: Ionic liquid encapsulated MIL-101 (Cr) based TFN membrane > original MIL-101 (Cr) based TFN membrane > pure PVDF substrate.

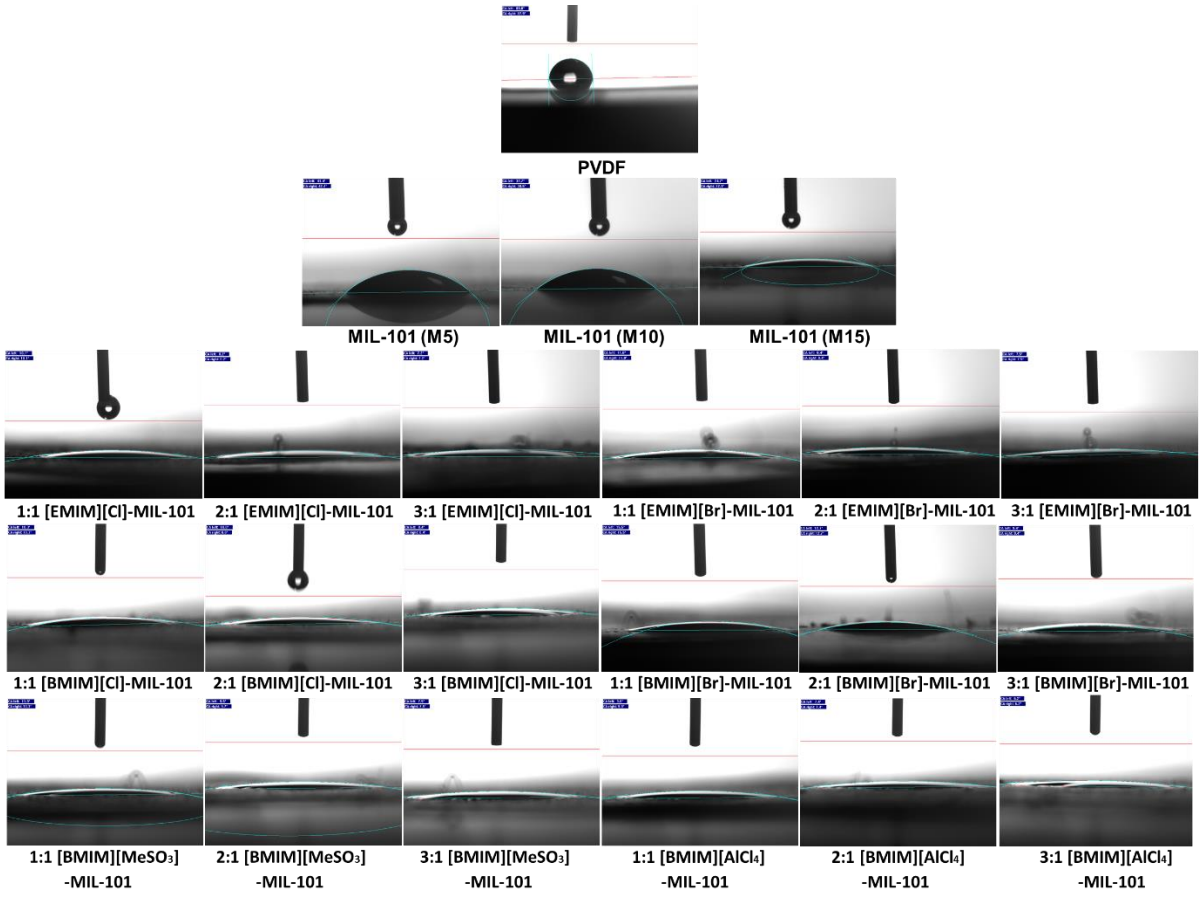

Figure S11: Water contact angle test for pure PVDF membrane and MIL-101 (Cr) based MOF TFN membranes.

Table S4: Water contact angle (CA) with different MOF based TFN membrane.

TFN membrane	CA left (°)	CA right (°)
Pure PVDF membrane	89.0	87.9
MIL-101 (5M)	41.4	42.4
MIL-101 (10M)	37.7	38.5
MIL-101 (15M)	24.7	22.3
1:1 [EMIM][Cl]-MIL-101	10.1	10.1
2:1 [EMIM][Cl]-MIL-101	8.2	8.2
3:1 [EMIM][Cl]-MIL-101	7.2	7.2
1:1 [EMIM][Br]-MIL-101	11.0	11.0
2:1 [EMIM][Br]-MIL-101	8.4	8.4
3:1 [EMIM][Br]-MIL-101	7.5	7.5
1:1 [BMIM][Cl]-MIL-101	10.3	10.3
2:1 [BMIM][Cl]-MIL-101	10.0	8.8
3:1 [BMIM][Cl]-MIL-101	8.4	8.4
1:1 [BMIM][Br]-MIL-101	15.5	15.5
2:1 [BMIM][Br]-MIL-101	12.7	12.7
3:1 [BMIM][Br]-MIL-101	9.4	9.4
1:1 [BMIM][$AlCl_4$]-MIL-101	9.6	9.9
2:1 [BMIM][$AlCl_4$]-MIL-101	7.4	7.4
3:1 [BMIM][$AlCl_4$]-MIL-101	6.2	6.2
1:1 [BMIM][$MeSO_3$]-MIL-101	11.9	10.3
2:1 [BMIM][$MeSO_3$]-MIL-101	9.5	9.7
3:1 [BMIM][$MeSO_3$]-MIL-101	7.5	7.5

S3. Separation performance of TFN membrane

Table S5 shows the diffusivity coefficient, solubility product constant (K_{sp}), Stokes radii and hydrated radius of metal ions [3-5].

Table S5. Diffusivity coefficient, solubility product constant (K_{sp}), Stokes radius and hydrated radius of Li^+, Mn^{2+}, Co^{2+} and Ni^{2+}.

Metal ion	Diffusivity coefficient (10^{-5} cm^2/s)	K_{sp} (of metal hydroxides at 25 °C)	Stokes radii (nm)	hydrated radius (nm)
Li^+	1.67	-	0.238	0.382
Mn^{2+}	1.43	1.9×10^{-13}	0.368	0.438
Co^{2+}	1.46	1.6×10^{-15}	0.335	0.423
Ni^{2+}	1.32	2.0×10^{-15}	0.292	0.404

Ageing test

Table S6 shows the calculated areas of characteristic ATR-FTIR bands for 2:1 [BMIM][$AlCl_4$]-MIL-101 based TFN membrane before and after filtration.

Table S6. Areas of characteristic ATR-FTIR bands for 2:1 [BMIM][$AlCl_4$]-MIL-101 based TFN membrane before and after filtration.

	Area (%.cm^{-1})				
FTIR bands (cm^{-1})	IL-MOF	IL-MOF after filtration :			
	fresh	1st	2nd	3rd	4th
660	194	201	189	171	171
747	475	472	447	433	420
829	92	97	94	87	90
1019	243	230	218	203	196
1166	136	134	122	113	113
1254	701	657	624	598	573
1284	601	575	545	519	503
1394	2656	2633	2465	2338	2271
1440	1120	1098	1062	1029	1011
1470	802	775	746	712	697
1618	2926	2859	2671	2488	2425
3396	7092	7008	6134	5311	5246

Separation with different feed solution and pH values

In this work, the pH of our LIB leaching solution is 3.51, and all the metal ion separation experiments are conducted around this pH value. This is because of that the mainly purpose of this work is to investigate the effect of the ILs encapsulation on the TFN membrane performance, only one type of LIB bio-leaching solution with certain pH (3.51) is chosen for evaluation purpose. Besides this feed solution, experiments using other feed solutions such as Co-rich LCO type LIB leaching solution (pH = 8.51) and Ni-rich NMC type LIB leaching solution (pH = 8.71) are also performed. The results are shown in Figure S12. The IL-MOF-based TFN membrane also shows promising separation effect. These experimental results prove that the as-fabricated membrane can work under a wide range of pH values. The effect of the pH on the separation performance will be one of our future research focus and is beyond the scope of this article.

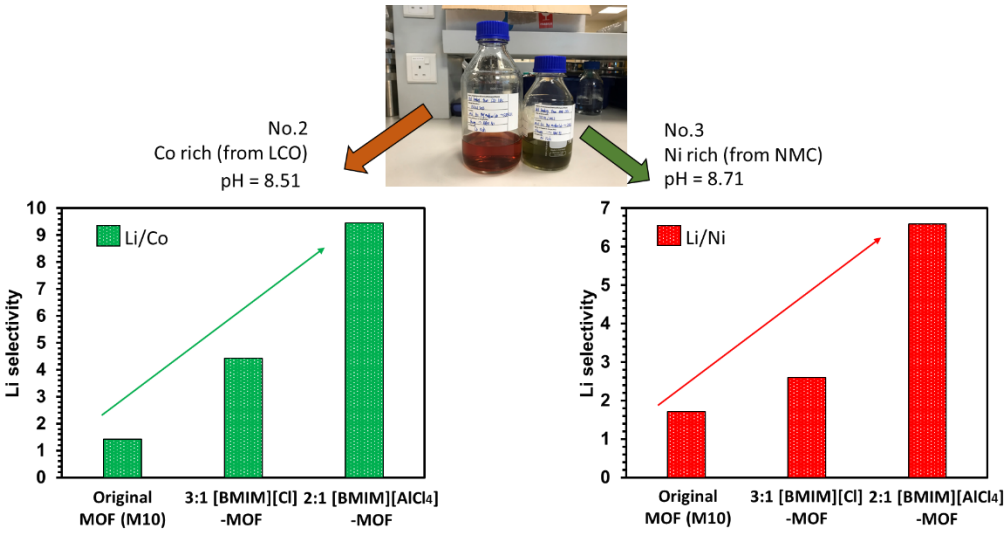

Figure S12: Metal ion separation performance with other feed solutions at different pH values.

Separation with PIP-TMC membranes

The separation performance of PIP-TMC membranes are shown in Figure S13, where almost no lithium separation effects are observed for Mn^{2+} ($S_{Li^+, Mn^{2+}} = 1.035$), Co^{2+} ($S_{Li^+, Co^{2+}} = 1.036$) and Ni^{2+} ($S_{Li^+, Ni^{2+}} = 1.028$).

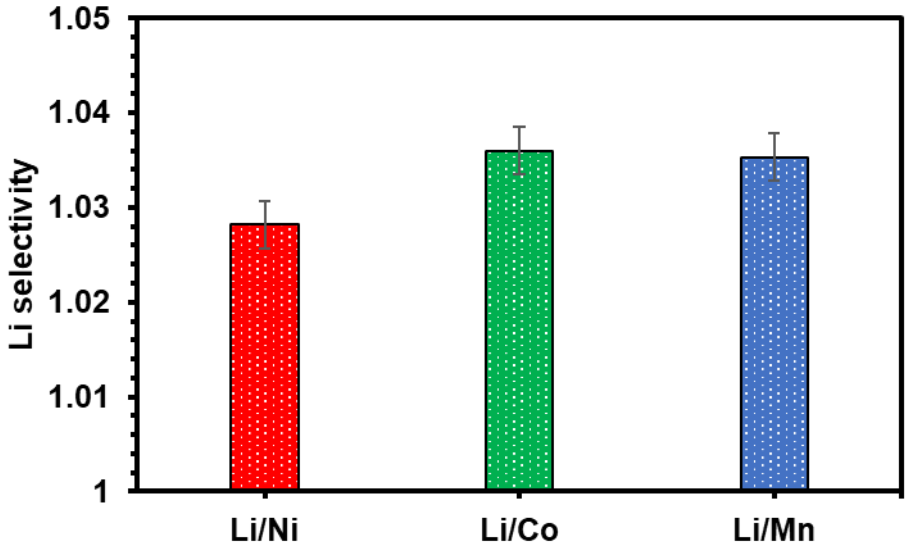

Figure S13: LIBs leaching solution separation with PIP-TMC membrane (without nanoparticle IL-MOFs).

S4. Additional characterization on MOF and TFN membrane

S4.1 PXRD (powder X-ray diffraction)

The XRD curves of the original and IL-modified MIL-101 (Cr) in this work are shown in Figure S14 (a) and (b), respectively. Comparable XRD profiles with evident intensity peaks are found with those reported in literature [6-8]. For comparison purpose, the XRD profile of MIL-101 (Cr) reported by Hou et al. [9] is shown in Figure S14 (c), where the major intensity peaks at ~ 8.2, 9.0, 16.3° are attributed to the diffractions of the (228), (135), and (5 9 13) planes. In addition, simulated XRD profile obtained from cif.file number 4000663 is shown in Figure S14 (d), where good agreement between the simulation and experimental profiles are observed within acceptable error range. It is noted that no standard card with PDF number is found in literature for MIL-101 (Cr). However, MIL-101 (Ti) with PDF (Powder Diffraction File) card 00-068-0703 is found and shown in Figure S14 (e). Based on the data provided in the database, the XRD profile is only plotted up to ~16.35°. Similar to the MIL-101-based MOF reported in this work, evident intensity peaks are found at ~5.1, 5.8, 8.1 and 8.9°. This is reasonable as the crystalline structures, phases and crystal orientations of MOF do not change significantly with only the change of metal/metal cluster type. The promising agreement of the XRD profiles reported in this work with that previously reported in literature indicates the successful synthesis and crystallization of MIL-101 (Cr) particles.

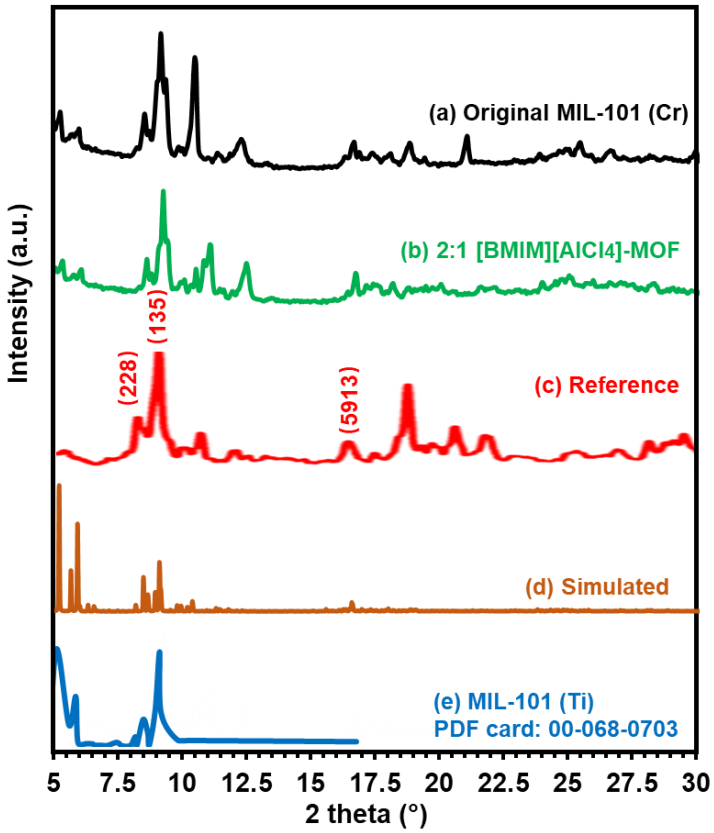

Figure S14: XRD profiles of (a) original MIL-101 (Cr) in this work, (b) IL-MIL-101 (Cr) in this work, (c) MIL-101 (Cr) from reference [9], (d) simulated XRD profile with cif.file number 4000663, and (e) MIL-101 (Ti) with PDF (Powder Diffraction File) card 00-068-0703.

S4.2 XPS (X-ray photoelectron spectroscopy)

XPS spectra of Cr element for the original and IL-modified MIL-101 (Cr) are shown in Figure S15, where evident characteristic peaks of Cr $2p_{1/2}$ and Cr$2p_{3/2}$ are found for both materials.

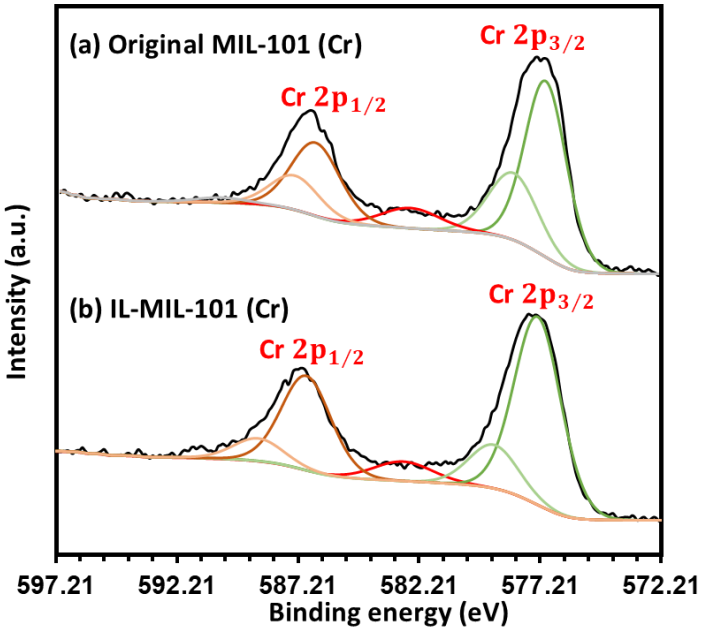

Figure S15: XPS spectra of Cr element for the original and IL-modified MIL-101 (Cr).

S4.3 Elemental composition analysis

S4.3.1 TFN membrane analysis by XPS

Based on the XPS characterization shown in Figure 3, the elemental composition analysis on the original and IL-modified MOF-based TFN membrane is shown in Table S7.

Table S7. Elemental composition analysis (atomic percentage) on the original and IL-modified MOF-based TFN membrane.

	C	N	O	Al	Cr
Original MOF-TFN membrane	21.56%	1.54%	46.96%	0.93%	21.56%
IL-MOF-TFN membrane	34.22%	3.53%	44.57%	2.23%	15.45%

S4.3.2 MOFs analysis by EDS/Elemental mapping

The elemental composition analysis on the original and IL-modified MOF is performed via EDS/elemental mapping technique, and the results are furnished in Table S8.

Table S8. Elemental composition analysis on the original and IL-modified MOF.

	C		N		O		Cr	
	Weight (%)	Atomic (%)	Weight (%)	Atomic (%)	Weight (%)	Atomic (%)	Weight (%)	Atomic (%)
Original MOF	47.05	59.68	0	0	37.47	35.68	14.94	4.39
IL-MOF	42.97	54.74	5.02	5.47	36.86	35.25	14.85	4.37

References

1. Wang, S., K. Gu, J. Wang, Y. Zhou, and C. Gao, *Enhanced the swelling resistance of polyamide membranes with reinforced concrete structure.* Journal of Membrane Science, 2019. **575**: p. 191-199.
2. Koutsou, C.P. and A.J. Karabelas, *Shear stresses and mass transfer at the base of a stirred filtration cell and corresponding conditions in narrow channels with spacers.* Journal of membrane science, 2012. **399**: p. 60-72.
3. Nightingale Jr, E., *Phenomenological theory of ion solvation. Effective radii of hydrated ions.* The Journal of Physical Chemistry, 1959. **63**(9): p. 1381-1387.
4. Agboola, O., J. Maree, R. Mbaya, C.M. Zvinowanda, G.F. Molelekwa, N. Jullok, B. Van der Bruggen, A. Volodine, and C. Van Haesendonck, *Deposition of toxic metal particles on rough nanofiltration membranes.* Korean Journal of Chemical Engineering, 2014. **31**(8): p. 1413-1424.
5. Haynes, W.M., D.R. Lide, and T.J. Bruno, *CRC handbook of chemistry and physics*. 2016: CRC press.
6. Tan, S.C. and H.K. Lee, *A hydrogel composite prepared from alginate, an amino-functionalized metal-organic framework of type MIL-101 (Cr), and magnetite nanoparticles for magnetic solid-phase extraction and UHPLC-MS/MS analysis of polar chlorophenoxy acid herbicides.* Microchimica Acta, 2019. **186**: p. 1-11.
7. Hassan, H.M., M.A. Betiha, S.K. Mohamed, E. El-Sharkawy, and E.A. Ahmed, *Stable and recyclable MIL-101 (Cr)–Ionic liquid based hybrid nanomaterials as heterogeneous catalyst.* Journal of Molecular Liquids, 2017. **236**: p. 385-394.
8. Luan, Y., Y. Qi, H. Gao, R.S. Andriamitantsoa, N. Zheng, and G. Wang, *A general post-synthetic modification approach of amino-tagged metal–organic frameworks to access efficient catalysts for the Knoevenagel condensation reaction.* Journal of Materials Chemistry A, 2015. **3**(33): p. 17320-17331.
9. Hou, P., G. Xing, D. Han, Y. Zhao, G. Zhang, H. Wang, C. Zhao, and C. Yu, *MIL-101 (Cr)/graphene hybrid aerogel used as a highly effective adsorbent for wastewater purification.* Journal of Porous Materials, 2019. **26**(6): p. 1607-1618.